metallic ground state are not inconsistent with the results of ref. 29, owing to the different surface preparation methods.

1. Shen, Z.-X. et al. Anomalously large gap anisotropy in the a–b plane of Bi₂Sr₂CaCu₂O₈₊ₓ. Phys. Rev. Lett. 70, 1553–1556 (1993).
2. Damascelli, A., Shen, Z. X. & Hussain, Z. Angle-resolved photoemission studies of the cuprate superconductors. Rev. Mod. Phys. 75, 473–541 (2003).
3. Emery, V. J. & Kivelson, S. A. Superconductivity in bad metals. Phys. Rev. Lett. 74, 3253–3256 (1995).
4. Honerkamp, C. & Lee, P. A. Staggered flux vortices and the superconducting transition in the layered cuprates. Phys. Rev. Lett. 92, 177002 (2004).
5. Chakravarty, S., Laughlin, R. B., Morr, D. K. & Nayak, C. Hidden order in the cuprates. Phys. Rev. B 63, 094503 (2001).
6. Tokura, Y. Colossal Magnetoresistive Oxides Ch. 1, 1 (Gordon & Breach Science, Amsterdam, 2000).
7. Dagotto, E. Nanoscale Phase Separation And Magnetoresistance (series eds Cardona, M. et al.) Ch. 2, 13 (Springer, Berlin/Heidelberg/New York, 2002).
8. Huang, X. Y., Mryasov, O. N., Novikov, D. L. & Freeman, A. J. Electronic and magnetic properties of layered colossal magnetoresistive oxides: La₂₋₂ₓSr₁₊₂ₓMn₂O₇. Phys. Rev. B 62, 13318–13322 (2000).
9. Dessau, D. S. et al. k-Dependent electronic structure, a large "ghost" Fermi surface, and a pseudogap in a layered magnetoresistive oxide. Phys. Rev. Lett. 81, 192–195 (1998).
10. Saitoh, T. et al. Temperature-dependent pseudogaps in colossal magnetoresistive oxides. Phys. Rev. B 62, 1039–1043 (2000).
11. Chuang, Y.-D., Gromko, A. D., Dessau, D. S., Kimura, T. & Tokura, Y. Fermi surface nesting and nanoscale fluctuating charge/orbital ordering in colossal magnetoresistive oxides. Science 292, 1509–1513 (2001).
12. Shen, K. M. et al. Nodal quasiparticles and antinodal charge ordering in Ca₂₋ₓNaₓCuO₂Cl₂. Science 307, 901–904 (2005).
13. Wells, B. O. et al. E versus k relations and many body effects in the model insulating copper oxide Sr₂CuO₂Cl₂. Phys. Rev. Lett. 74, 964–967 (1995).
14. Ronning, F. et al. Anomalous high-energy dispersion in angle-resolved photoemission spectra from the insulating cuprate Ca₂CuO₂Cl₂. Phys. Rev. B 71, 094518 (2005).
15. Shen, K. M. et al. Missing quasiparticles and the chemical potential puzzle in the doping evolution of the cuprate superconductors. Phys. Rev. Lett. 93, 267002 (2004).
16. Mishchenko, A. S. & Nagaosa, N. Electron-phonon coupling and a polaron in the t-J model: from the weak to the strong coupling regime. Phys. Rev. Lett. 93, 036402 (2004).
17. Rosch, O. & Gunnarsson, O. Dispersion of incoherent spectral features in systems with strong electron-phonon coupling. Eur. Phys. J. B 43, 11–18 (2005).
18. Perebeinos, V. & Allen, P. B. Franck-Condon-broadened angle-resolved photoemission spectra predicted in LaMnO₃. Phys. Rev. Lett. 85, 5178–5181 (2000).
19. Engelsberg, S. & Schrieffer, J. R. Coupled electron-phonon system. Phys. Rev. 131, 993–1008 (1963).
20. Yoshida, T. et al. Metallic behaviour of lightly doped La₂₋ₓSrₓCuO₄ with a Fermi surface forming an arc. Phys. Rev. Lett. 91, 027001 (2003).
21. Kaminski, A. et al. Renormalization of spectral line shape and dispersion below Tᶜ in Bi₂Sr₂CaCu₂O₈₊δ. Phys. Rev. Lett. 86, 1070–1073 (2001).
22. Moritomo, Y., Asamitsu, A., Kuwahara, H. & Tokura, Y. Giant magnetoresistance of manganese oxides with a layered perovskite structure. Nature 380, 141–144 (1996).
23. Palstra, T. T. M. et al. Transport mechanisms in doped LaMnO₃: evidence for polaron formation. Phys. Rev. B 56, 5104–5107 (1997).
24. Vasiliu-Doloc, L. et al. Charge melting and polaron collapse in La₁.₂Sr₁.₈Mn₂O₇. Phys. Rev. Lett. 83, 4393–4396 (1999).
25. Campbell, B. J. et al. Structure of nanoscale polaron correlations in La₁.₂Sr₁.₈Mn₂O₇. Phys. Rev. B 65, 014427 (2001).
26. Millis, A. J., Littlewood, P. B. & Shraiman, B. I. Double exchange alone does not explain the resistivity of La₁₋ₓSrₓMnO₃. Phys. Rev. Lett. 74, 5144–5147 (1995).
27. Hanaguri, T. et al. A 'checkerboard' electronic crystal state in lightly hole-doped Ca₂₋ₓNaₓCuO₂Cl₂. Nature 430, 1001–1005 (2005).
28. Mitchell, J. F. et al. Charge delocalization and structural response in layered La₂₋₂ₓSr₁₊₂ₓMn₂O₇: Enhanced distortion in the metallic regime. Phys. Rev. B 55, 63–66 (1997).
29. Freeland, J. W. et al. Full bulk polarization and intrinsic tunnel barriers at the surface of layered manganites. Nature Mater. 4, 62–67 (2005).

LETTERS

Probing carrier dynamics in nanostructures by picosecond cathodoluminescence

M. Merano[1], S. Sonderegger[1], A. Crottini[1], S. Collin[1], P. Renucci[1], E. Pelucchi[1], A. Malko[1], M. H. Baier[1], E. Kapon[1], B. Deveaud[1] & J.-D. Ganière[1]

Picosecond and femtosecond spectroscopy allow the detailed study of carrier dynamics in nanostructured materials[1]. In such experiments, a laser pulse normally excites several nanostructures at once. However, spectroscopic information may also be acquired using pulses from an electron beam in a modern electron microscope, exploiting a phenomenon called cathodoluminescence. This approach offers several advantages. The multimode imaging capabilities of the electron microscope enable the correlation of optical properties (via cathodoluminescence) with surface morphology (secondary electron mode) at the nanometre scale[2]. The broad energy range of the electrons can excite wide-bandgap materials, such as diamond- or gallium-nitride-based structures that are not easily excited by conventional optical means. But perhaps most intriguingly, the small beam can probe a single selected nanostructure. Here we apply an original time-resolved cathodoluminescence set-up to describe carrier dynamics within single gallium-arsenide-based pyramidal nanostructures[3] with a time resolution of 10 picoseconds and a spatial resolution of 50 nanometres. The behaviour of such charge carriers could be useful for evaluating elementary components in quantum computers[4,5], optical quantum gates[6] or single photon sources[7–9] for quantum cryptography[10].

It is of primary importance to understand as precisely as possible how the charge carriers behave in a single nano-object[11,12]. Standard optical techniques, such as fluorescence microscopy, provide a spatial resolution that remains limited to a fraction of a micrometre. More sophisticated techniques, like near-field optical microscopy, can be used to gain spectroscopic information at the 100-nanometre scale, but do not routinely provide adequate time resolution[13] when faint secondary signals, such as luminescence, have to be measured. Moreover, the performances of ultraviolet optics limit the use of these techniques to materials with a gap lower than 4 eV.

Modern electron microscopes represent a direct approach for determining surface morphology of semiconducting nanostructures with a spatial resolution of a few nanometres. Using the cathodoluminescence imaging mode, that is, an excitation of the luminescence via the electron beam of the microscope, we gain access to spectroscopic information within a single nano-object and correlation with the surface morphology is straightforward[14]. More than 20 years ago, Steckenborn et al.[15] proposed a new set-up allowing the addition of temporal resolution to cathodoluminescence. Beam blanking was achieved by deflecting the electron beam away from the axis of the electron optical column, using a set of deflection plates. Even if this experimental technique made it possible to obtain interesting results[16–20], it suffers from some disadvantages: the beam always sweeps the sample and the minimum pulse length is a few tens of nanoseconds. The semiconductor is then excited in steady state and the temporal information is obtained during the decay of the luminescence only, with a temporal resolution not better than a few hundred picoseconds.
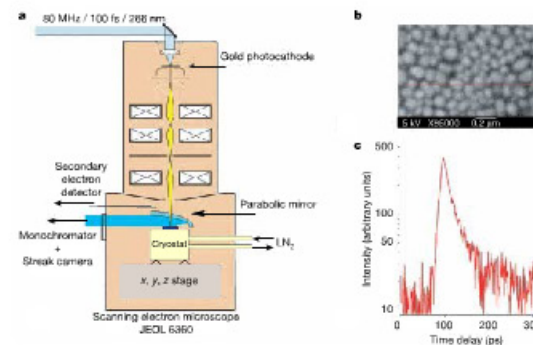

Figure 1 | Set-up, and spatial and temporal resolution. a, Schematic implementation of our time-resolved cathodoluminescence system. b, Secondary electron images of gold nanoparticles deposited on an amorphous carbon film. The spatial resolution on such a specimen is estimated to be better than 50 nm. The spatial resolution in secondary electron mode is mainly determined by the size of the electron probe onto the specimen. c, Time-resolved spectra of a GaN specimen at room temperature. From the rise time of the signal, the temporal width of the electron pulse is estimated to be about 10 ps.

[1]Institute of Quantum Electronics and Photonics, Ecole Polytechnique Fédérale de Lausanne, CH-1015 Lausanne-EPFL, Switzerland.

To overcome these drawbacks, we developed a new cathodoluminescence set-up, allowing us to keep the main advantages of the scanning electron microscope, that is, the multi-imaging mode capabilities, and to improve the pulsed electron gun. We use an optically driven electron gun[21–24] similar to the one used to probe chemical changes by ultrafast electron diffraction[25].

To implement our idea we have replaced the classical hairpin tungsten electron gun of a JEOL 6360 scanning electron microscope (Fig. 1a) with a 20-nm-thick gold photocathode deposited on a quartz plate. By illuminating the photocathode (in transmission mode) by a ultraviolet mode-locked laser (266 nm, 200 fs, 80.7 MHz of repetition rate, spot size radius of 3 μm), we generate a pulsed electron beam, bright enough (average brightness of 2×10^3 A cm^{-2} steradians^{-1}, 1–100 pA at the specimen surface) to allow secondary electron images to be recorded, thus allowing us to identify the nanostructures under study. A streak camera (Hamamatsu 5680), mounted behind a monochromator (spectral resolution better than 200 μeV) is used as a time-resolved detector (in photon-counting mode). A liquid-nitrogen cryostat is used to cool the sample down to 90 K. Observations on a specimen made of gold particles deposited on an amorphous carbon film confirmed that this modified microscope has a spatial resolution of the secondary electron images of better than 50 nm (Fig. 1b). Careful measurements on a reference GaN specimen demonstrate an electron pulse width of about 10 ps (Fig. 1c). The average number of electrons per pulse is generally lower than ten (a beam current of 13 pA corresponds to one electron per pulse) still allowing us to realize secondary electron images of the specimen. We note here that a single electron per pulse still allows a large signal because, depending on the acceleration voltage, each electron may generate a few thousand electron–hole pairs into the sample. To estimate the potentiality of this new set-up, we choose to investigate GaAs-based pyramidal nanostructures.

Our choice is dictated by the interest of such structures both in the field of basic research and for a number of possible applications. Pyramidal quantum dots (QDs) naturally provide site control, a wide choice in the possible densities, excellent optical properties, high uniformities and flexible energy tuning[3,9,26]. The simultaneous presence of several nanostructures in one single pyramid has attracted the interest of innovative theoretical proposals for quantum information protocols[27]. The samples were fabricated with the following

procedure: before growth, a GaAs substrate is patterned with a 5-μm pitch hexagonal matrix of tetrahedral recesses, using standard photolithography and wet etching[5]. Growth of InGaAs/AlGaAs heterostructures by low-pressure organo-metallic chemical vapour deposition is then performed on the patterned substrate. The growth process results in the formation of different nanostructures, as sketched and defined in Fig. 2.

All measurements have been performed at 90 K and an acceleration voltage of 10 kV. The cathodoluminescence spectrum from a single pyramid (obtained with a pulsed excitation and with a time-integrated detection) and spectrally resolved images taken at wavelengths corresponding to the different recombination channels are presented in Fig. 3. Some of the peaks in the spectrum were identified on the basis of previous optical studies, through their energy position and the cathodoluminescence image[26].

Importantly, the cathodoluminescence images relative to QDs, quantum wires (QWRs), and vertical quantum wires (VQWRs) (Fig. 2) cannot be directly related to the nanostructure location at the origin of the luminescence signal. This is typical for cathodoluminescence experiments because the emission pattern does not depend only on the primary electron diffusion range, but also on the carrier transport processes in these complex nanostructures. If we consider, for example, the cathodoluminescence image at the QD wavelength, we observe that the emission pattern spans the entire pyramid. This means that carriers created at any point of the pyramid find a path to diffuse towards the dot. One of the main advantages of time-resolved cathodoluminescence is that it allows us to unveil the specificities of this carrier transport. We can excite at any point of interest and gain information in the spectral, spatial and temporal domains. As an example, results obtained when we excited at the centre of one of the pyramid faces are presented in Fig. 4.

To give more quantitative estimates on the carrier diffusion properties within the structure, we have excited the pyramid at carefully chosen points (three along an edge and three points onto the face of the pyramid) and we have detected in parallel the signals corresponding to the different recombination channels (see Fig. 2): QD, VQWR, QWR, quantum well (QW) and vertical quantum well (VQW). Typical results for the VQW and the QWR are depicted in
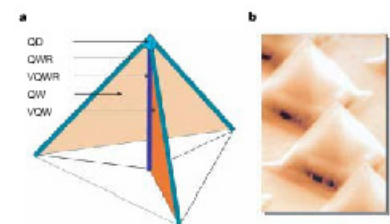

Figure 4 | Streak image. Typical time traces corresponding to the different nanostructures of the pyramid, when excited in the middle of one of the faces of this pyramid. The different curves are labelled according to the related structure. The five different nanostructures display very different time behaviours that are signatures of the complex transport mechanisms within the pyramid.

Fig. 5 for six different excitation points within the pyramid. The sensitivity of the method is directly demonstrated by the large differences observed between the different traces, both in terms of intensities and in terms of dynamics.

Full analysis of the data allows us to obtain a very detailed understanding of the carrier dynamics inside these pyramids. The electron–hole pairs are created within a volume of 300 nm around the impact point of the electrons, that is, mostly in the AlGaAs barriers of the structure. From there, they diffuse to the closest nanostructure, which is often one of the VQWs or the QWRs. This process occurs through diffusion, with a diffusivity of about 10 cm^2 s^{-1} corresponding to an ambipolar mobility of the order of 1,000 cm^2 V^{-1} s^{-1}, and to a trapping time shorter than our experimental resolution. This explains in particular the 150-ps rise time observed for the QWR luminescence. The carriers in the VQW get trapped in the QWR within a typical time of less than 100 ps, and then diffuse towards the central structures (the VQWR and the QD) in the QWR. We show in Fig. 6 the results of our diffusion model for three different excitation points along the edge of the pyramid, allowing us to limit the numbers of parameters for the fit. The model allows us to deduce a mobility of 1,400 cm^2 V^{-1} s^{-1} along the wire, and a negligible quantum mechanical trapping time into the VQWR. In the case of Figs 5 and 6, owing to the high mobility in the selected pyramid, saturation effects are observed both in the VQWR and in the QD. Indeed, even if we excite at the level of one electron per pulse, this electron creates enough pairs in the structure to allow this because the QD can only accommodate two pairs, and the VQWR about ten pairs.

Thus we have developed a new spectroscopic tool, a picosecond time-resolved cathodoluminescence system with a time resolution of

Figure 2 | InGaAs/AlGaAs pyramidal quantum structures. a, Schematic representation of the five heterostructures present in an InGaAs/AlGaAs pyramid (the AlGaAs cap layer is not represented on the scheme). An InGaAs quantum dot (QD; typically 30 nm in lateral size) connected to several types of low-dimensional barriers: three InGaAs quantum wires (QWRs) on the edges of the pyramid, three InGaAs quantum wells (QWs) on the pyramid faces, and three vertical quantum wells (VQWs) and a vertical quantum wire (VQWR) located at the intersection of the vertical quantum wells. **b,** Scanning electron microscope picture of the pyramid (the top of the pyramids are separated by 5 μm). The final step of the process is a back etching to remove the substrate.
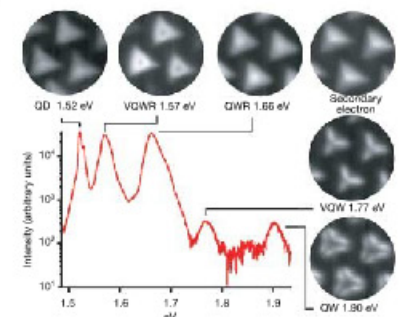

Figure 3 | Cathodoluminescence spectrum and images. Cathodoluminescence characterization of our sample. The spectrum shows five main peaks corresponding to the five main structures in the pyramid. These are, from low to high energy, the quantum dot at the tip of the pyramid (QD), the vertical quantum wire (VQWR), the lateral quantum wires (QWR) the vertical quantum wells (VQW) and the quantum well along the sides of the pyramid (QW).
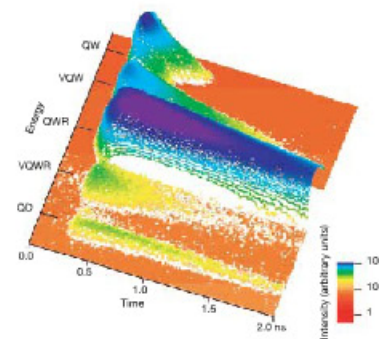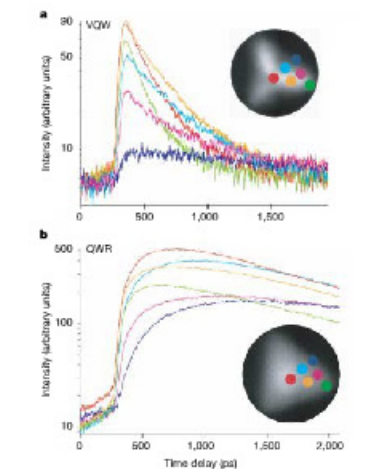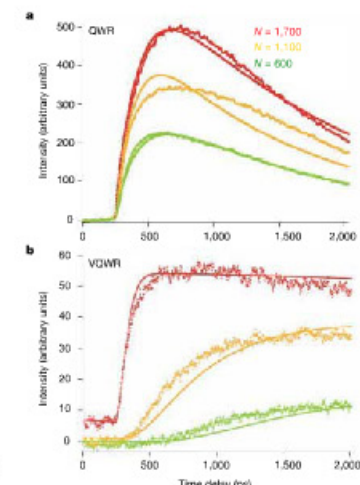

Figure 5 | Luminescence temporal profiles versus excitation points. Time traces corresponding to the VQW (a) and the QWR (b) for the different excitation points depicted in the inset. From such traces we can directly deduce that: (1) the carrier injection in the VQW and the QWR is more efficient when we excite on the pyramid edge; (2) the rise time for the QWR basically corresponds to the decay time of the VQW; and (3) long delays are observed when excited on the side of the pyramid resulting from the longer diffusion path.

Figure 6 | QWR and VQWR fits. Fits to the time traces of the QWR (a) and the VQWR (b), with basically one single fitting parameter: the ambipolar diffusion coefficient of the carriers within the QWR. Saturation of the VQWR as well as the very long radiative and non-radiative lifetimes is clearly shown on the upper curve of Fig. 6.

the order of 10 ps, together with a spatial resolution of 50 nm. This system allows us to study the carrier dynamics inside GaAs back-etched pyramids, and obtain a precise knowledge of the photoexcited carrier path towards the lower-energy state: the dot at the tip of the pyramid.

1. Shah, J. *Ultrafast Spectroscopy of Semiconductors and Semiconductor Nanostructures* Ch. 8 (Springer, Berlin, 1999).
2. Reimer, L. *Scanning Electron Microscopy* Ch. 1 (Springer, Berlin, 1998).
3. Kapon, E. *et al.* Site- and energy-controlled pyramidal quantum dot heterostructures. *Physica E* 25, 288–297 (2004).
4. Loss, D. & DiVincenzo, D. P. Quantum computation with quantum dots. *Phys. Rev. A* 57, 120–126 (1998).
5. Imamoglu, A. Are quantum dots useful for quantum computation? *Physica E* 16, 47–50 (2003).
6. Li, X. *et al.* An all-optical quantum gate in a semiconductor quantum dot. *Science* 301, 809–811 (2003).
7. Benson, O., Santori, C., Pelton, M. & Yamamoto, Y. Regulated and entangled photons from a single quantum dot. *Phys. Rev. Lett.* 84, 2513–2516 (2000).
8. Gerard, J. M. & Gayral, B. Strong Purcell effect for InAs quantum boxes in three-dimensional solid-state microcavities. *J. Lightwave Technol.* 17, 2089–2095 (1999).
9. Baier, M. H. *et al.* Single photon emission from site-controlled pyramidal quantum dots. *Appl. Phys. Lett.* 84, 648–650 (2004).
10. Gisin, N., Ribordy, G. G., Tittel, W. & Zbinden, H. Quantum cryptography. *Rev. Mod. Phys.* 74, 145–195 (2002).
11. Warburton, R. J. Self-assembled semiconductor quantum dots. *Contemp. Phys.* 43, 351–364 (2002).
12. Korovyanko, O. J., Sheng, C. X., Vardeny, Z. V., Dalton, A. B. & Baughman, R. H. Ultrafast spectroscopy of excitons in single-walled carbon nanotubes. *Phys. Rev. Lett.* 92, 017403 (2004).
13. Gustafsson, A., Pistol, M. E., Montelius, L. & Samuelson, L. Local probe techniques for luminescence studies of low-dimensional semiconductor structures. *J. Appl. Phys.* 84, 1715–1775 (1998).
14. Mernigen, J., Jahn, U., Brandt, O., Yang, H. & Ploog, K. Identification of optical transitions in cubic and hexagonal GaN by spatially resolved cathodoluminescence. *Phys. Rev. B* 53, 1881–1885 (1996).
15. Steckenborn, A., Munzel, H. & Bimberg, D. Cathodoluminescence lifetime pattern of GaAs-surfaces around dislocations. *J. Lumin.* 24–5, 351–354 (1981).
16. Bell, A. *et al.* Exciton freeze-out and thermally activated relaxation at local potential fluctuations in thick Al_xGa_{1-x}N layers. *J. Appl. Phys.* 95, 4670–4674 (2004).
17. Vetter, U., Hofsass, H. & Taniguchi, T. Visible cathodoluminescence from Eu-implanted single- and polycrystal c-BN annealed under high-temperature, high-pressure conditions. *Appl. Phys. Lett.* 84, 4286–4288 (2004).
18. Diaz-Guerra, C., Piqueras, J., Castaldini, A., Cavallini, A. & Polenta, L. Time-resolved cathodoluminescence and photocurrent study of the yellow band in Si-doped GaN. *J. Appl. Phys.* 94, 2341–2346 (2003).
19. Turck, V. *et al.* Time-resolved spectroscopy of single quantum dots: Evidence for phonon-assisted carrier feeding. *Phys. Status Solidi B* 224, 643–647 (2001).
20. Zhang, X., Rich, D. H., Kobayashi, J. T., Kobayashi, N. P. & Dapkus, P. D. Carrier relaxation and recombination in an InGaN/GaN quantum well probed with time-resolved cathodoluminescence. *Appl. Phys. Lett.* 73, 1430–1432 (1998).
21. Elsayedali, H. E. & Herman, J. W. Ultrahigh-vacuum picosecond laser-driven electron-diffraction system. *Rev. Sci. Instrum.* 61, 1636–1647 (1990).
22. May, P., Halbout, J. M. & Chiu, G. Picosecond photoelectron scanning electron-microscope for noncontact testing of integrated-circuits. *Appl. Phys. Lett.* 51, 145–147 (1987).
23. Kong, S. H., Kinnosswright, J., Nguyen, D. C., Sheffield, R. L. & Weber, M. E. Performance of cesium telluride photocathodes as an electron source for the Los-Alamos advanced fel. *Nucl. Instrum. Methods A* 358, 284–286 (1995).
24. Siwick, B. J., Dwyer, J. R., Jordan, R. E. & Miller, R. J. D. An atomic-level view of melting using femtosecond electron diffraction. *Science* 302, 1382–1385 (2003).
25. Williamson, J. C., Cao, J. M., Ihee, H., Frey, H. & Zewail, A. H. Clocking transient chemical changes by ultrafast electron diffraction. *Nature* 386, 159–162 (1997).
26. Hartmann, A., Ducommun, Y., Kapon, E., Hohenester, U. & Molinari, E. Few-particle effects in semiconductor quantum dots: Observation of multicharged excitons. *Phys. Rev. Lett.* 84, 5648–5651 (2000).
27. Piermarocchi, C., Chen, P., Sham, L. J. & Steel, D. G. Optical RKKY interaction between charged semiconductor quantum dots. *Phys. Rev. Lett.* 89, 167402 (2002).
28. Leifer, K., Hartmann, A., Ducommun, Y. & Kapon, E. Carrier transport and luminescence in inverted-pyramid quantum structures. *Appl. Phys. Lett.* 77, 3923–3925 (2000).

LETTERS

Impacts of orbital forcing and atmospheric carbon dioxide on Miocene ice-sheet expansion

Ann Holbourn[1], Wolfgang Kuhnt[1], Michael Schulz[2] & Helmut Erlenkeuser[3]

The processes causing the middle Miocene global cooling, which marked the Earth's final transition into an 'icehouse' climate about 13.9 million years ago (Myr ago)[1–4], remain enigmatic. Tectonically driven circulation changes[5,6] and variations in atmospheric carbon dioxide levels[7,8] have been suggested as driving mechanisms, but the lack of adequately preserved sedimentary successions has made rigorous testing of these hypotheses difficult. Here we present high-resolution climate proxy records, covering the period from 14.7 to 12.7 million years ago, from two complete sediment cores from the northwest and southeast subtropical Pacific Ocean. Using new chronologies through the correlation to the latest orbital model[9], we find relatively constant, low summer insolation over Antarctica coincident with declining atmospheric carbon dioxide levels and ice-sheet expansion and global cooling, suggesting a causal link. We surmise that the thermal isolation of Antarctica played a role in providing sustained long-term climatic boundary conditions propitious for ice-sheet formation. Our data document that Antarctic glaciation was rapid, taking place within two obliquity cycles, and coincided with a striking transition from obliquity to eccentricity as the drivers of climatic change.

About 13.9 Myr ago, the Earth's climate cooled dramatically after an extended period of relative warmth. This key transition in the Earth's climatic and biotic evolution marked the final stage of stepwise Cenozoic cooling, and coincided with major ice-sheet expansion over Antarctica[1–4]. However, the timing, duration and driving mechanisms of this critical episode still remain largely unsolved, because sedimentary successions spanning this interval have been strongly affected by carbonate dissolution or burial diagenesis or proved incomplete owing to radical changes in ocean circulation. Thus, developing uninterrupted, high-resolution middle Miocene climate records that can be tied to an orbital timescale represents a major challenge for understanding the pacing and trigger of Cenozoic global cooling.

Here we present benthic foraminiferal oxygen ($\delta^{18}O$) and carbon ($\delta^{13}C$) isotope (4–5 kyr resolution) and X-ray fluorescence scanning (XRF) records (1-kyr resolution) in complete middle Miocene sedimentary sequences recovered at Ocean Drilling Program (ODP) Site 1146 (19° 27.40′ N, 116° 16.37′ E, 2,092 m) and Site 1237 (16° 0.421′ S, 76° 22.685′ W, 3,212 m) (Supplementary Information). These continuous successions allow unprecedented resolution of climate evolution on orbital timescales and permit detailed correlation of palaeoceanographic events in spatially separated regions in the northwest and southeast subtropical Pacific.

We developed orbitally tuned age models (Supplementary Information) by correlating the $\delta^{18}O$ records at each site to computed variations of the Earth's orbit and solar insolation (obliquity and eccentricity in ref. 9). The most salient features of the $\delta^{18}O$ time series are the major increase in values at 13.91–13.84 Myr ago (0.8‰ at Site 1237 and 1.2‰ at Site 1146), and the transition from high-amplitude obliquity-paced variations dominant between 14.7 and 13.9 Myr ago to eccentricity-paced fluctuations between 13.8 and 13.1 Myr ago (Figs 1 and 2). Higher-amplitude oscillations at Site 1146 (0.56‰ ± 0.12‰ versus 0.31‰ ± 0.15‰ mean amplitude at Site 1237) indicate a stronger temperature component in the 1146 $\delta^{18}O$ record between 14.7 and 13.9 Myr ago. Nevertheless, the global correlation of isotopic events and evidence for substantial Antarctic ice growth between 14.8 and 13.6 Myr ago[10] support that both $\delta^{18}O$ records closely track ice-volume fluctuations. Furthermore, benthic Mg/Ca temperature estimates indicate that most of the deep-sea $\delta^{18}O$ increase at 13.91–13.84 Myr ago can be attributed to an increase in continental ice volume[11]. The 100-kyr and 41-kyr signal components in $\delta^{18}O$ show amplitude modulation similar to that of the eccentricity and obliquity, with a striking transition from high amplitude in the 41-kyr band to high amplitude in the 100-kyr band at ~14.1–13.8 Myr ago (Fig. 2). The 100-kyr beat is also prominent in the 1237 Fe record after 14.1 Myr ago.

At first sight, the middle Miocene transition from a 41-kyr to 100-kyr world shows similarity to the 'Middle Pleistocene revolution' following an increase in Northern Hemisphere glaciation[12–14]. However, the middle Miocene transition differs in several aspects: (1) the middle Miocene 100-kyr cycles do not exhibit higher-amplitude variations than the 41-kyr cycles; (2) the transition from 41-kyr to 100-kyr periodicity occurred during or even before ice-sheet expansion without substantial time lag; (3) the middle Miocene 100-kyr cycles show a clear phase relationship and amplitude modulation to eccentricity, as well as both 125-kyr and 95-kyr components (Fig. 1, Supplementary Fig. S4). In contrast, the origin of the middle Pleistocene 100-kyr cycles remains puzzling, because their onset coincided with a period of weak eccentricity forcing[15].

Between 14.7 and 13.9 Myr ago, high amplitude in the 41-kyr band of the $\delta^{18}O$ signal (Fig. 2) suggests an already expanded Antarctic ice-sheet fluctuating in response to obliquity forcing. The ensuing $\delta^{18}O$ increase at 13.91–13.84 Myr ago, which marked the main increase in middle Miocene Antarctic glaciation, was also clearly modulated by obliquity (Figs 1 and 3). Obliquity controls the gradient in summer insolation between high and low latitudes, which drives the poleward atmospheric heat and moisture transfer[16]. Enhanced meridional moisture transport during periods of high differential heating between high and low latitudes at obliquity minima would promote ice-sheet growth, whereas a low summer insolation gradient at obliquity maxima would decrease poleward moisture transport, inhibiting ice-sheet build-up[16,17]. Similar obliquity-paced variations in moisture supply for the Holocene and late Pleistocene East Antarctic ice-sheet are evident from the deuterium excess record in the Vostok ice core[18]. High deuterium excess values during obliquity

[1]Institute of Geosciences, Christian-Albrechts-University, D-24118 Kiel, Germany. [2]Department of Geosciences and Research Center Ocean Margins, University of Bremen, Postfach 330 440, D-28334 Bremen, Germany. [3]Leibniz Laboratory for Radiometric Dating and Stable Isotope Research, Christian-Albrechts-University, D-24118 Kiel, Germany.